JETIR.ORG

## JOURNAL OF EMERGING TECHNOLOGIES AND

INNOVATIVE RESEARCH (JETIR)

An International Scholarly Open Access, Peer-reviewed, Refereed Journal

# Aluminium Substitution-Driven Modulation of Structural properties in Dysprosium Iron Garnet Nanoparticle

Samyak milind Bansode, Shaikh Taufiq Khalil Ahemad, Archana D. Chapolikar, V.D.Murumkar \* Department of Physics, Deogiri College, Chhatrapati Sambhaji Nagar 431001, MS, India

#### **Abstract**

Nanocrystalline samples of DyFe<sub>5-x</sub>Al<sub>x</sub>O<sub>12</sub> (x = 0.0 and 1.0) were synthesized using the sol-gel method to investigate the structural effects of aluminum substitution in the garnet lattice. X-ray diffraction (XRD) confirmed the formation of single-phase cubic garnet structures across all compositions, with slight peak shifts and crystallite size reduction indicative of doping-induced lattice strain. Scanning electron microscopy confirmed the nanoscale morphology and compositional control, with average particle sizes decreasing from 46.8 to 34.9 nm. The results demonstrate that Al<sup>3+</sup> incorporation offers a viable route to tune the microstructural properties of DyIG-based garnets for advanced applications.

Keywords: Garnet; Nanomaterials; Structural properties; Elastic properties

#### 1.Introduction:

Rare-earth iron garnets (R<sub>3</sub>Fe<sub>5</sub>O<sub>12</sub>, where R = rare earth element) constitute an important class of magnetic oxide materials that exhibit a rich array of physical properties including high magneto-optical activity, low dielectric loss, high saturation magnetization, and structural stability.[1, 2] Among these, dysprosium iron garnet (Dy<sub>3</sub>Fe<sub>5</sub>O<sub>12</sub> or DyIG) has received considerable attention for applications in microwave devices, magnetic sensors, magneto-optical recording media, and biomedical fields such as targeted drug delivery and hyperthermia therapy.[3, 4] The garnet structure, characterized by a cubic lattice (space group Ia-3d), accommodates cations at three distinct

crystallographic sites dodecahedral (Dy<sup>3+</sup>), octahedral, and tetrahedral (Fe<sup>3+</sup>) allowing for a high degree of chemical flexibility and tunability of physical properties through targeted ionic substitutions.[5, 6]

The substitution of Fe<sup>3+</sup> ions in the garnet structure with non-magnetic or weakly magnetic cations is an effective strategy for modifying the electronic, magnetic, and mechanical characteristics of the material. In particular, the partial replacement of Fe<sup>3+</sup> with aluminium (Al<sup>3+</sup>), a non-magnetic trivalent ion with a larger ionic radius and lower electronegativity, is known to induce significant changes in the magnetic anisotropy, lattice dynamics, and local bonding environment of the garnet matrix.[7, 8] Aluminium typically prefers octahedral coordination, and its incorporation disrupts the Fe–O–Fe super exchange interactions, thereby altering the internal lattice strain, phonon spectra, and mechanical stiffness.[9, 10] Furthermore, Al<sup>3+</sup> substitution can lead to grain refinement and enhanced surface homogeneity due to its influence on diffusion kinetics and local coordination environments during synthesis.[11, 12]

In nanostructured garnets, the reduction in particle size introduces additional surface effects, quantum confinement, and defect states that markedly influence their magnetic and optical responses. Therefore, exploring the combined effects of cation substitution and nanoscale morphology is essential for developing advanced garnet-based materials with tailored functionalities. The sol-gel method offers a versatile and cost-effective route to synthesize nanocrystalline garnets with precise control over composition, homogeneity, and particle size. Compared to conventional solid-state techniques, the sol-gel process promotes uniform mixing at the molecular level, reduces reaction temperature, and facilitates the formation of high-purity phases with minimal energy input.

In this study, DyFe<sub>5-x</sub>Al<sub>x</sub>O<sub>12</sub> (x = 0.0 and 1.0) nanoparticles were synthesized via the sol-gel method to systematically investigate the structural, vibrational, elastic, and morphological consequences of aluminium doping. A comprehensive suite of characterization techniques including X-ray diffraction (XRD) and scanning electron microscopy (SEM) was employed to elucidate the influence of Al<sup>3+</sup> substitution on lattice parameters, crystallite size and particle morphology.

This work contributes to a deeper understanding of how chemical doping and nanostructuring synergistically affect the fundamental properties of garnet materials, paving the way for their use in suitable device application.

#### 2.0 Methods and Materials:

Aluminium-substituted Dysprosium iron garnet, with the general formula DyFe<sub>5-x</sub>Al<sub>x</sub>O<sub>12</sub> (x = 0.0 and 1.00) was synthesized via a sol-gel combustion route using high-purity precursors. Dysprosium (III) nitrate hexahydrate [Dy(NO<sub>3</sub>)<sub>3</sub>·6H<sub>2</sub>O, Sigma-Aldrich, 99.9%], Aluminium (III) nitrate hexahydrate [Al(NO<sub>3</sub>)<sub>3</sub>·6H<sub>2</sub>O, Acros Organics, 99.9%], and ferric nitrate nonahydrate [Fe(NO<sub>3</sub>)<sub>3</sub>·9H<sub>2</sub>O, Acros Organics, 99.9%] were used as cation sources. Citric acid monohydrate (Acros, 99.9%) was added as a chelating agent and fuel. All precursors were dissolved in 100 mL of deionized water under constant magnetic stirring. Aqueous ammonia solution was added dropwise to the solution to adjust the pH to approximately 7, ensuring neutral sol formation. The homogeneous mixture was continuously stirred and heated at 90 °C to promote evaporation, leading to gel formation. The resulting gel was further dried at 250 °C to initiate combustion, yielding a foamy ash-like powder. This powder was pressed into pellets of approximately 1 g using a uniaxial press under 5-ton pressure, producing discs with a diameter of 10 mm and a thickness of about 0.4 mm. All compositions were annealed at 1150 °C for 10 hours to achieve phase crystallization. This post-annealing treatment is considered analogous to a solid-state reaction, enhancing phase purity and crystallinity.

The structural and phase analysis of the synthesized powders was carried out using a Rigaku Ultima IV X-ray diffractometer (XRD) with CuK $\alpha$  radiation ( $\lambda = 1.5404$  Å). Microstructural features of sintered pellets were examined using field emission scanning electron microscopy (FESEM; JEOL JSM-6360 and MIRA-3 LMH).

### 3.1 X-ray Diffraction (XRD) Analysis:

X-ray diffraction (XRD) patterns of DyFe<sub>5-x</sub>Al<sub>x</sub>O<sub>12</sub> (x = 0.0 and 1.0) samples were recorded to confirm phase formation, determine crystallographic structure, and evaluate various microstructural parameters (Figure 1). Samples exhibit sharp and well-defined diffraction peaks corresponding to the garnet phase, indexed to characteristic planes such as (400), (420), (422), (521), and (444), confirming the formation of a single-phase cubic garnet structure without any secondary impurity phases.[13, 14]

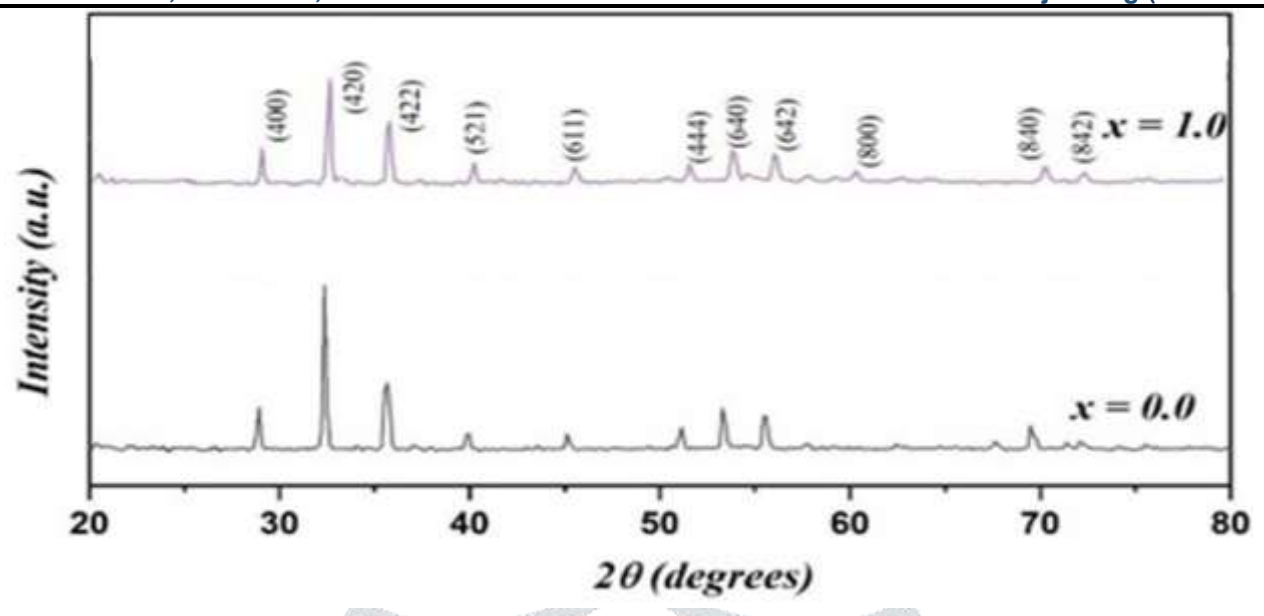


Figure 1: XRD patterns of DyFe<sub>5-x</sub>Al<sub>x</sub>O<sub>12</sub> (x = 0.0 and 1.0)

The most intense diffraction peak corresponds to the (400) plane, and its shift toward higher 20 values with increasing Al content suggests a minor contraction of the lattice due to the substitution of Fe<sup>3+</sup> (ionic radius ~0.67 Å) with the smaller Al<sup>3+</sup> ions (~0.53Å). However, non-linear variations in the lattice constant and unit cell volume are observed, likely due to complex structural relaxation and strain compensation within the lattice.

The average crystallite size (D) was estimated using the Debye-Scherrer formula:[15]

$$D = \frac{0.9\lambda}{\beta \cos \theta} \tag{1}$$

where  $\beta$  is the full width at half maximum (FWHM) in radians,  $\theta$  is the Bragg angle, and  $\lambda$  is the X-ray wavelength (1.5406 Å for Cu K $\alpha$  radiation).

The lattice parameter (a) was calculated using Bragg's law:[16]

$$a = d\sqrt{h^2 + k^2 + l^2} \tag{2}$$

where d is the interplanar spacing and (hkl) are the Miller indices. and the cubic relation:

$$V = a^3 \tag{3}$$

Additionally, the microstrain ( $\epsilon$ ), dislocation density ( $\delta$ ), and specific surface area (SSA) were calculated using the following formulas:

$$\varepsilon = \frac{\beta}{4tan\theta} \tag{4}$$

Dislocation density:  $\delta = \frac{1}{D^2}$ 

Specific surface area = 
$$\frac{6}{D \times Q}$$
 (6)

Table 1: Variation of Crystallite Size, Lattice Constant, Microstrain, Dislocation Density, Specific Surface Area, and Unit Cell Volume with Al Content (x) in DyFe<sub>5-x</sub>Al<sub>x</sub>O<sub>12</sub> Garnet Nanoparticles

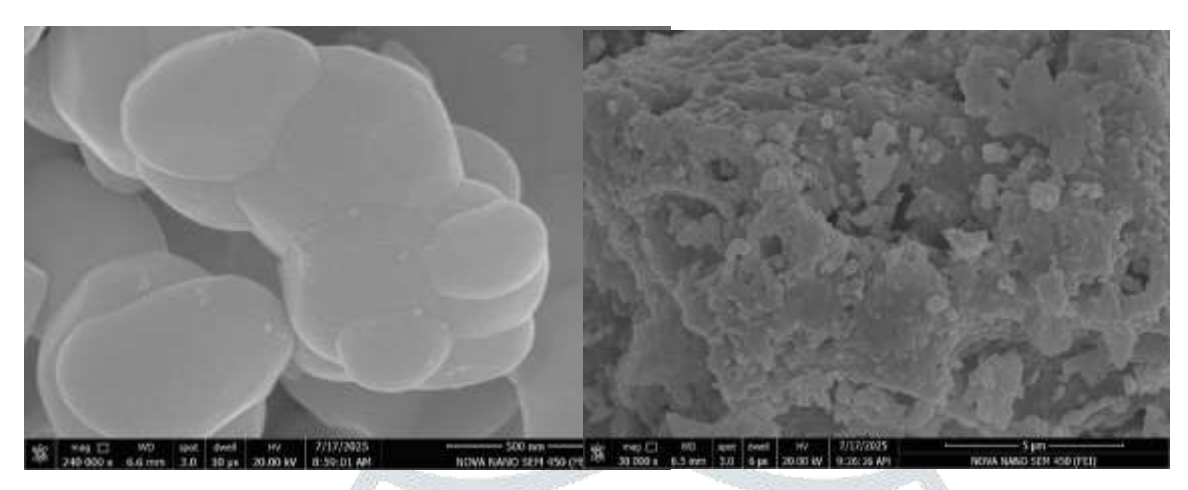
x	D (nm)	a (Å)	ε (×10 <sup>-3</sup> )	$\delta (\times 10^{14} \mathrm{m}^{-2})$	$SSA\ (m^2/g)$	$V(\mathring{A}^3)$
0.00	46.80	12.41	2.88	4.57	24.65	1913.27
1.00	39.21	12.39	3.87	6.50	29.43	1902.87

Crystallite Size, Lattice Constant, Microstrain, Dislocation Density, Specific Surface Area, and Unit Cell Volume with Al Content (x) in DyFe<sub>5-x</sub>Al<sub>x</sub>O<sub>12</sub> Garnet Nanoparticles are listed in table 1. The crystallite size decreases from 46.80 nm (x = 0.0) to 39.21 nm (x = 1.0), indicating that Al<sup>3+</sup> doping introduces lattice strain and impedes grain growth. The lattice parameter remains nearly constant with subtle variation, reflecting the structural robustness of the garnet lattice despite ionic substitution. The microstrain and dislocation density increase with Al doping, indicating an accumulation of lattice distortions and defects. The SSA increases with decreasing D, favoring applications such as catalysis or sensors where high surface area is beneficial.

The variation of structural and microstructural parameters with Al content (x) in DyFe<sub>5-x</sub>Al<sub>x</sub>O<sub>12</sub> garnet nanoparticles reveals significant insights into the influence of doping on the material's crystallinity and lattice dynamics. The microstrain ( $\epsilon$ ) increases initially, peaking at x = 0.25 (5.60 × 10<sup>-3</sup>), and then fluctuates, reflecting the generation and accommodation of strain within the lattice. Correspondingly, the dislocation density ( $\delta$ ) increases with Al content, indicating a rise in crystallographic defects as crystallite size decreases. The specific surface area (SSA) also increases from 24.65 m<sup>2</sup>/g (x = 0.0) to 29.43 m<sup>2</sup>/g (x = 1.0), consistent with finer crystallites offering more surface exposure. The unit cell volume (V) fluctuates slightly, suggesting structural distortion due to Al incorporation. Overall, these trends confirm that Al doping systematically modifies the microstructure and enhances defect concentration, which can be tailored for applications requiring high surface area and controlled grain size.

#### 3.2. SEM Analysis:

Figure 2: SEM micrographs of DyFe<sub>5-x</sub>Al<sub>x</sub>O<sub>12</sub>, where (left) x = 0.0, and (right) (b) x = 1.0.



The surface morphology and grain structure of DyFe<sub>5-x</sub>Al<sub>x</sub>O<sub>12</sub> nanoparticles were examined using Scanning Electron Microscopy (SEM), with representative micrographs shown for all compositions ranging from x = 0.0 and x = 1.0 (Figure 2). The SEM images reveal that the synthesized garnet powders exhibit a generally spherical to sub-spherical morphology with moderate agglomeration, which is a common feature in ferrite systems prepared via solid-state or sol-gel methods. The agglomeration can be attributed to the high surface energy of the nanosized crystallites and magnetic interactions among them.

Across all compositions, the particles are distributed over a relatively broad size range, which is further quantified by grain size histograms extracted from the SEM micrographs. The particle sizes observed from SEM are consistently larger than those estimated by XRD, confirming the presence of polycrystalline agglomerates composed of smaller crystallites. This discrepancy is expected, as SEM captures entire particles (including agglomerates), whereas XRD provides information at the crystallite scale.

For the undoped sample (x = 0.0), the average particle size is relatively large, with most grains in the range of 50–70 nm. As aluminium concentration increases, a gradual refinement of the grain morphology is observed. At higher substitution levels (x = 1.0), the morphology begins to change subtly. The particles become more irregular and agglomerated, with certain regions showing enhanced densification or localized sintering. This behavior could be attributed to local structural relaxation, surface energy minimization, or phase stabilization mechanisms associated with the increased aluminium content.[17] Interestingly, the slight increase in XRD crystallite size at x = 1.0

coincides with the formation of these more compact structures, indicating partial grain growth or fusion due to reduced internal strain.

The histogram analyses for each composition reveal a narrowing of the particle size distribution with increasing x, suggesting improved homogeneity at moderate doping levels (Figure 3). The narrowing may be linked to enhanced nucleation kinetics and suppressed grain growth induced by the presence of aluminium, which may act as a growth-inhibiting dopant by occupying octahedral sites and introducing local strain fields.

The SEM analysis confirms that aluminium substitution plays a significant role in modifying the morphological characteristics of DyFe<sub>5</sub>O<sub>12</sub> nanoparticles. The observed decrease in average particle size and enhanced surface uniformity at intermediate doping levels are consistent with the XRD findings, which indicate increased microstrain and defect concentration. These morphological improvements, particularly the increase in specific surface area due to smaller and more uniform particles, may enhance the functional performance of these materials in applications such as catalysis, microwave absorption, or biomedical delivery, where surface reactivity and uniformity are critical.

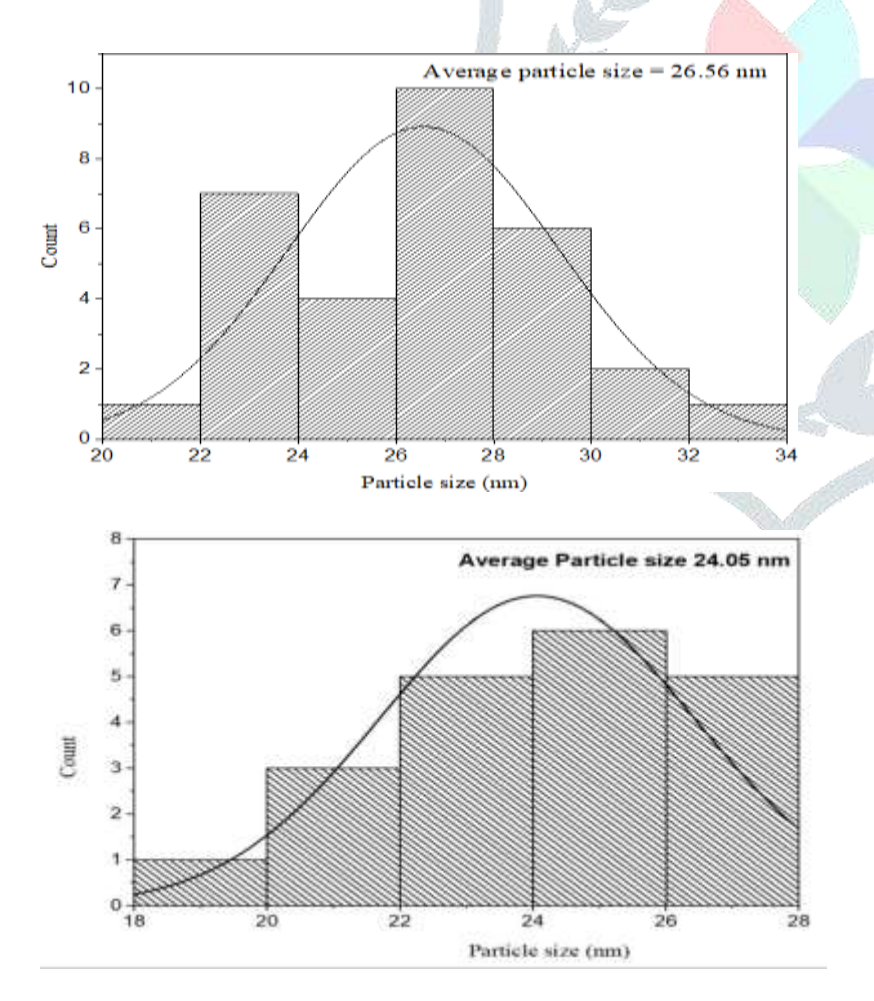


Figure 3: Histogram extracted from SEM micrographs of DyFe<sub>5-x</sub>Al<sub>x</sub>O<sub>12</sub>, where (left) x = 0.0, and (right) x = 1.0.

#### **Conclusions:** 4.

This study presents a detailed investigation into the impact of aluminium substitution on the structural properties of nanocrystalline DyFe<sub>5-x</sub>Al<sub>x</sub>O<sub>12</sub> garnets synthesized via the sol-gel route. XRD analysis confirmed the stability of the cubic garnet phase across the entire doping range, while variations in lattice constants, microstrain, and crystallite size revealed the subtle influence of Al<sup>3+</sup> on lattice dynamics. Electron microscopy analysis corroborated the crystallographic findings and revealed well-defined nanoparticle morphologies with improved uniformity at intermediate doping levels. Overall, the findings provide valuable insight into structure–property relationships in doped garnet systems and establish DyFe<sub>5-x</sub>Al<sub>x</sub>O<sub>12</sub> as a promising candidate for device applications.

#### **References:**

- [1] S. Geller, J. Remeika, R. Sherwood, H. Williams, G. Espinosa, Magnetic study of the heavier rareearth iron garnets, Physical Review, 137 (1965) A1034.
- [2] R. Nakamoto, B. Xu, C. Xu, H. Xu, L. Bellaiche, Properties of rare-earth iron garnets from first principles, Physical Review B, 95 (2017) 024434.
- [3] M. Phan, M. Morales, C. Chinnasamy, B. Latha, V. Harris, H. Srikanth, Magnetocaloric effect in bulk and nanostructured Gd3Fe5O12 materials, Journal of Physics D: Applied Physics, 42 (2009) 115007.
- [4] L. Jiang, S. Yang, M. Zheng, H. Chen, A. Wu, Synthesis and magnetic properties of nanocrystalline Gd3Fe5O12 and GdFeO3 powders prepared by sol-gel auto-combustion method. Materials research bulletin, 104 (2018) 92-96.
- [5] J. Waerenborgh, D. Rojas, A. Shaula, V. Kharton, F. Marques, Defect formation in Gd3Fe5O12-based garnets: a Mössbauer spectroscopy study, Materials Letters, 58 (2004) 3432-3436.
- [6] H. Lassri, E. Hlil, S. Prasad, R. Krishnan, Magnetic and electronic properties of nanocrystalline Gd3Fe5O12 garnet, Journal of solid state chemistry, 184 (2011) 3216-3220.
- [7] R. Nazlan, M. Hashim, I.R. Ibrahim, F.M. Idris, I. Ismail, W.N.W. Ab Rahman, N.H. Abdullah, M.M.M. Zulkimi, M.S. Mustaffa, Indium-substitution and indium-less case effects on structural and magnetic properties of yttrium-iron garnet, Journal of Physics and Chemistry of Solids, 85 (2015) 1-12.
- [8] S. Naik, A. Salker, Variation in the magnetic moment of Indium doped Ce0. 1Y2. 9Fe5O12 garnet relative to the site inversion, Journal of alloys and compounds, 600 (2014) 137-145.
- [9] J.A. Pardoe, A.J. Downs, Development of the chemistry of indium in formal oxidation states lower than+ 3, Chemical reviews, 107 (2007) 2-45.
- [10] L.N. Hutfluss, Studies in Pure and Transition Metal Doped Indium Oxide Nanocrystals, in, University of Waterloo, 2015.
- [11] M.P. Ghosh, P. Kumar, M. Kar, S. Mukherjee, Impact of In3+ ion substitution on microstructural, magnetic and dielectric responses of nickel-cobalt spinel ferrite nanocrystals, Journal of Materials Science: Materials in Electronics, 31 (2020) 17762-17772.
- [12] R. Nazlan, M. Hashim, I.R. Ibrahim, F. Mohd Idris, W.N. Wan Ab Rahman, N.H. Abdullah, I. Ismail, S. Kanagesan, Z. Abbas, R.S. Azis, Influence of indium substitution and microstructure changes on the magnetic properties evolution of Y3Fe5- xlnxO12 (x= 0.0-0.4), Journal of Materials Science: Materials in Electronics, 26 (2015) 3596-3609.
- [13] S. Zanatta, L. Cótica, A. Paesano Jr, S. De Medeiros, J. Da Cunha, B. Hallouche, Mechanosynthesis of gadolinium iron garnet, Journal of the American Ceramic Society, 88 (2005) 3316-3321.
- [14] T. Ramesh, R. Shinde, S. Murthy, Nanocrystalline gadolinium iron garnet for circulator applications, Journal of magnetism and magnetic materials, 324 (2012) 3668-3673.

- [15] U. Holzwarth, N. Gibson, The Scherrer equation versus the Debye-Scherrer equation, Nature nanotechnology, 6 (2011) 534-534.
- [16] J. Robertson, Elements of X-ray diffraction by BD Cullity, in, International Union of Crystallography, 1979.
- [17] A. Walsh, C.R.A. Catlow, Structure, stability and work functions of the low index surfaces of pure indium oxide and Sn-doped indium oxide (ITO) from density functional theory, Journal of Materials Chemistry, 20 (2010) 10438-10444.

